



# Electrochemical capacitance of mesoporous tungsten oxynitride in aqueous electrolytes

Olga Kartachova<sup>a</sup>, Alexey M. Glushenkov<sup>a,\*</sup>, Yanhui Chen<sup>b</sup>, Hongzhou Zhang<sup>b</sup>, Xiujuan J. Dai<sup>a</sup>, Ying Chen<sup>a</sup>

<sup>a</sup> Institute for Frontier Materials (IFM), Deakin University, Waurn Ponds, VIC 3216, Australia

<sup>b</sup> School of Physics, Centre for Research on Adaptive Nanostructures and Nanodevices (CRANN), Trinity College Dublin, Dublin 2, Ireland

## H I G H L I G H T S

- Tungsten oxynitride  $W_{0.75}(N,O)$  is evaluated as an electrode material for supercapacitors.
- The electrochemical properties of  $W_{0.75}(N,O)$  are studied in aqueous electrolytes.
- Maximum capacitance is observed in  $H_2SO_4$  electrolyte and maximum stability is found in KOH electrolyte.
- The contribution of a pseudocapacitive charge storage mechanism is proposed.

## A R T I C L E I N F O

### Article history:

Received 5 May 2012

Received in revised form

10 July 2012

Accepted 31 July 2012

Available online 9 August 2012

### Keywords:

Supercapacitors

Pseudocapacitance

Cyclic stability

Oxynitrides

Aqueous electrolytes

## A B S T R A C T

Transition metal nitrides and oxynitrides are promising candidates for the application in electrodes of supercapacitors. In this manuscript characterization of tungsten oxynitride and its electrochemical properties in a range of aqueous electrolytes (1 M  $H_2SO_4$ , 1 M KOH, 3 M KCl, 3 M NaCl, 1 M LiCl and 1 M  $CaCl_2$ ) are presented. The electrochemical behavior of tungsten oxynitride depends strongly on the type of cation present in the electrolyte, and the highest capacitance value of  $85 \text{ F g}^{-1}$  is measured in 1 M  $H_2SO_4$ . Cyclic stability in the acid, neutral and alkaline electrolytes is evaluated, and the highest stability is observed in 1 M KOH electrolyte. Possible charge–discharge mechanisms are discussed, and the contribution of a pseudocapacitive mechanism in addition to the electric double-layer formation is proposed.

© 2012 Elsevier B.V. All rights reserved.

## 1. Introduction

Supercapacitors are electrochemical energy storage devices possessing high power densities with a large range of high-power applications in the industrial, residential and transportation sectors [1,2]. Examples of their application include power backup systems, braking energy recovery and engine starting in hybrid electric vehicles, collection and storage of the energy from renewable and alternating energy sources such as solar lanterns, and other uses where the energy is needed in the pulse form [1–4]. The market for supercapacitors has been growing rapidly in the last 20 years, with worldwide sales revenue expected to increase from \$40 million in 1989 to an estimated \$877 million in 2014 [1].

\* Corresponding author. Tel.: +61 3 5227 2931; fax: +61 3 52271103.  
E-mail address: [alexey.glushenkov@deakin.edu.au](mailto:alexey.glushenkov@deakin.edu.au) (A.M. Glushenkov).

Today, commercially available supercapacitors are predominantly electrochemical double-layer capacitors (EDLCs) with carbon-based electrode materials due to the low cost, high surface area and the availability of carbons [2,4]. EDLCs store the charge in the electrical double-layer (EDL) at the electrodes/electrolyte interface. This double-layer is the result of the electrostatic separation of ion and electron charges [5]. However, typical capacitance values achieved in carbon-based materials through the EDL charge storage process are only  $20\text{--}50 \text{ }\mu\text{F cm}^{-2}$  [5,6]. In contrast to the EDL mechanism, another possible storage mechanism, pseudocapacitive charge storage, involves the Faradaic charge transfer processes across the electrodes/electrolyte interface and leads to the change in the valence states of the active electrode material [5]. Pseudocapacitive processes allow additional charge storage due to the higher energy density associated with the Faradaic reactions. Therefore, capacitance values per electrode area are often 10–100 times higher when compared to the EDLC mechanism [5,7–9].

The benchmark material exhibiting the pseudocapacitive charge storage mechanism is  $\text{RuO}_2$ , with specific capacitance values over  $700 \text{ F g}^{-1}$  (approximately  $1000 \text{ } \mu\text{F cm}^{-2}$ ) due to the amorphous form of hydrous ruthenium oxide ( $\text{RuO}_2 \cdot x\text{H}_2\text{O}$ ) [8]. However, the wide application of ruthenium oxide is limited by the high cost of ruthenium; therefore, alternative materials need to be explored. Many compounds, including transition metal oxides [9,10], conducting polymers [11] and a few transition metal nitrides [12–16] have been investigated as potential candidates for pseudocapacitive electrode materials.

The most popular alternative to  $\text{RuO}_2$  is manganese oxide  $\text{MnO}_2$  because of a much more attractive cost and lower toxicity. Manganese oxides with various crystalline forms, morphologies and degrees of crystallinity have been tested, and an ideal pseudocapacitive behavior in aqueous electrolytes has been found with capacitances varying from approximately 150 to above  $350 \text{ F g}^{-1}$  [17–26]. The proposed charge storage mechanisms of manganese oxides include the reversible surface adsorption of protons and cations from the electrolyte [18,26] or their incorporation into the oxide lattice [22–24], with the simultaneous transition between the  $\text{Mn}^{4+}$  and  $\text{Mn}^{3+}$  valence states. Manganese oxide can exist in various crystalline and amorphous forms [27–29] and it has been demonstrated that the pseudocapacitive behavior of manganese oxides in aqueous electrolytes depends on the type of the present cation as well as on the crystalline phase of the material [19–21,25,27–29]. It has previously been suggested that poorly crystallized  $\text{MnO}_2$  rather follows pseudocapacitive chemisorption mechanism, while crystalline phases mostly involve ion intercalation into the crystal lattice [27]. The inherent drawback of  $\text{MnO}_2$  is its limited rate capability due to the poor electronic conductivity. Efforts have been devoted to overcome this deficiency by preparing electrodes in the form of thin films [30,31] or composites with carbon materials [32,33]. In such optimized electrode configurations, capacitance values above  $1000 \text{ F g}^{-1}$  have been achieved [30]. However, these approaches can suffer from several shortcomings. More specifically, the thin films have a low active material content and the composites suffer from limited energy density. In order to improve the conductivity of the electrodes without compromising the active material content and the energy density, nanostructured materials with high intrinsic conductivity should be investigated.

Transition metal nitrides and oxynitrides possess unique physico-chemical properties, such as the combination of metallic conductivity and high chemical resistance in corrosive media [34], which enable transition metal nitrides and oxynitrides to be considered as promising candidates for application in supercapacitors. Several transition metal nitrides, including VN [14], TiN [16] and  $\gamma\text{-Mo}_2\text{N}$  [12,13,15] have been successfully used in supercapacitor electrodes, which demonstrated significant capacitance values of  $1340 \text{ F g}^{-1}$  for VN [14],  $111 \text{ F g}^{-1}$  for  $\gamma\text{-Mo}_2\text{N}$  [13] and  $238 \text{ F g}^{-1}$  for TiN [16] at a scan rate of  $2 \text{ mV s}^{-1}$ .

In this study, tungsten oxynitride is investigated for possible application in the supercapacitor electrodes. The article presents the phase identification of the synthesized tungsten oxynitride by X-ray diffraction, transmission electron microscopy and electron energy loss spectroscopy, as well as the morphological characterization by scanning electron microscopy and low temperature  $\text{N}_2$  adsorption. The electrochemical properties of tungsten oxynitride are studied in a range of aqueous electrolytes ( $1 \text{ M H}_2\text{SO}_4$ ,  $1 \text{ M KOH}$ ,  $3 \text{ M KCl}$ ,  $3 \text{ M NaCl}$ ,  $1 \text{ M LiCl}$  and  $1 \text{ M CaCl}_2$ ) and the possible contribution of the pseudocapacitive charge storage is discussed.

## 2. Experimental

Tungsten oxynitride was synthesized by a temperature-programmed reduction of tungsten (VI) oxide (Fluka, 95410) in

$\text{NH}_3$  atmosphere [35]. Half a gram of  $\text{WO}_3$  was loaded in an alumina crucible and placed in a conventional tube furnace (Tetlow Kilns & Furnaces Pty Ltd, Australia). Prior to the heating, the furnace tube was purged with argon gas to remove air. The furnace was subsequently heated to  $700^\circ\text{C}$  at a heating rate of  $180^\circ\text{C h}^{-1}$ , kept at this temperature for 2 h and then cooled down to the room temperature. The flow rate of  $\text{NH}_3$  was fixed to  $0.2 \text{ l min}^{-1}$  throughout this process. Prior to the exposure to air, the sample was passivated by passing a special mixture of gases ( $\text{Ar}$  with  $0.1 \text{ vol.}\% \text{ O}_2$ ) over the sample for 1 h at a flow rate of  $0.5 \text{ l min}^{-1}$ .

The synthesized oxynitride powder was examined using X-ray diffraction (XRD, PANalytical X'Pert PRO diffractometer with  $\text{Cu K}\alpha$  radiation ( $\lambda = 0.15418 \text{ nm}$ )). The scanning electron microscopy (SEM) measurements were performed using a Carl Zeiss SUPRA 55VP electron microscope. Surface area and pore size distribution were measured by low temperature  $\text{N}_2$  adsorption using a Micro-metrics Tristar 3000 system. The surface area was calculated by the Branauer–Emmett–Teller (BET) method and the pore size distribution was calculated by the Barrett–Joiner–Helenda (BJH) method from the  $\text{N}_2$  adsorption isotherm.

For transmission electron microscope (TEM) characterization, an FEI Titan instrument operated at  $300 \text{ kV}$  and equipped with a scanning transmission electron microscopy (STEM) unit, a Gatan Image Filter (GIF) and an energy dispersive X-ray (EDX) spectrometer was used. Electron energy loss spectra (EELS) were collected from nanosized areas of the specimen in TEM nanoprobe diffraction mode with a  $2 \text{ mm}$  entrance aperture and a spectrometer channel resolution of  $0.1 \text{ eV}$ . The convergence and collection angles were approximately  $9.0 \text{ mrad}$  and  $2.9 \text{ mrad}$ , respectively, with a short acquisition time of  $10\text{--}20 \text{ s}$  to minimize beam damage. For energy-filtered TEM (EFTEM) imaging, a three-window method was employed to acquire tungsten, nitrogen, and oxygen elemental distributions.

X-ray photoelectron spectroscopy (XPS) was used to investigate the surface characteristics of the samples. The XPS spectra were obtained using an X-ray photoelectron spectrometer from Thermo Fischer Scientific using monochromatic  $\text{K}\alpha$  X-rays focused to a  $400 \text{ } \mu\text{m}$  spot size. Excessive charging of the samples was minimized using a flood gun; furthermore, binding energies of elements were accurately corrected by assigning the energy of  $284.6 \text{ eV}$  to the component of the  $\text{C } 1\text{s}$  peak with the lowest energy. Survey spectra were obtained at a pass energy of  $100 \text{ eV}$  while high resolution peak scans were performed at a pass energy of  $20 \text{ eV}$ . Additional peak scans were employed to obtain spectra of W, O, N, C, S, K and Cl elements.

In order to test the electrochemical performance of tungsten oxynitride, galvanostatic charge/discharge and cyclic voltammetry methods were applied. A three electrode cell with an  $\text{Ag}/\text{AgCl}$  or  $\text{Hg}/\text{HgO}$  electrode as a reference electrode and a Pt wire as a counter electrode was used. Potentiostat/galvanostat (Solartron Analytical 1470E) was used for the measurements. The analysis was performed in  $1 \text{ M H}_2\text{SO}_4$ ,  $1 \text{ M KOH}$ ,  $3 \text{ M KCl}$ ,  $3 \text{ M NaCl}$ ,  $1 \text{ M LiCl}$  and  $1 \text{ M CaCl}_2$  aqueous electrolytes. Electrode slurry was prepared by mixing  $85 \text{ wt.}\%$  of the synthesized tungsten oxynitride powder with  $10 \text{ wt.}\%$  carbon nanopowder (Sigma–Aldrich, #699632) and  $5 \text{ wt.}\%$  poly(vinylidene)fluoride (PVDF, Sigma–Aldrich) in NMP (N-methyl-2-pyrrolidone, anhydrous,  $99.5\%$ , Sigma–Aldrich). The slurry was mixed in an agate mortar and coated onto titanium foil. The coated electrode was oven dried at  $90^\circ\text{C}$ . The amount of the coated material after drying was between  $3$  and  $4 \text{ mg cm}^{-2}$ . Cells were filled with electrolytes under vacuum. The capacitance values were calculated from the galvanostatic charge and discharge curves.

In order to prepare charged and discharged electrodes for XRD analysis, galvanostatic charge–discharge cycling was conducted

within the potential window of  $-0.4$  to  $0.5$  V in  $1$  M  $\text{H}_2\text{SO}_4$  and from  $-0.8$  to  $0.2$  V in  $3$  M KCl electrolytes vs the Ag/AgCl reference electrode. The cycling process was stopped after ten cycles at the potentials of  $-0.4$  or  $0.5$  V in  $1$  M  $\text{H}_2\text{SO}_4$  and  $-0.8$  or  $0.2$  V in  $3$  M KCl, respectively. The electrodes were then cleaned with the deionized water and dried in the air at the room temperature.

### 3. Results and discussion

The morphological characterization of the synthesized sample reveals that the powder is composed of  $20\text{--}30$   $\mu\text{m}$  particles (Fig. 1a). The higher magnification image (Fig. 1b) indicates that the material has a porous structure, with a discernible pore size of less than  $20$  nm. Nitrogen adsorption measurement (Fig. 2) confirms that the particles are mesoporous and the pore size distribution, estimated by the BJH method, is centered around  $5$  nm. Virtually no pores bigger than  $14$  nm are detected, which is consistent with the information obtained from SEM images (Fig. 1b). The specific surface area, measured by the BET method, is  $42\text{ m}^2\text{ g}^{-1}$ .

Phase identification of the synthesized material was performed using X-Ray diffraction and TEM techniques. The XRD pattern (Fig. 3) shows six diffraction peaks located at  $30.1^\circ$ ,  $37.5^\circ$ ,  $43.7^\circ$ ,  $63.4^\circ$ ,  $76.1^\circ$  and  $80.1^\circ$  and fitting the diffraction lines of  $\text{W}_3\text{N}_4$  (Powder Diffraction File #: 75-1002) or  $\text{W}_{0.75}(\text{N},\text{O})$  (PDF #: 25-1255). The presence of a slope in the background of the XRD spectrum is due to the signal from the sample holder.

The TEM results are presented in Fig. 4. A bright field image (Fig. 4a) shows that the sample is composed of nanocrystals of approximately  $3\text{--}8$  nm diameters. The corresponding electron diffraction pattern (Fig. 4b) indicates a polycrystalline diamond cubic structure with  $a = 0.413$  nm. Fig. 4c and d show a high resolution TEM image and a high angle annular dark-field (HAADF) image, respectively. The lattice fringes resolved in the high-resolution TEM image correspond to the (001) and (110) planes of a cubic crystal, and the [011] direction is the zone axis in this image. The HAADF image clearly identifies the porosity in the material.

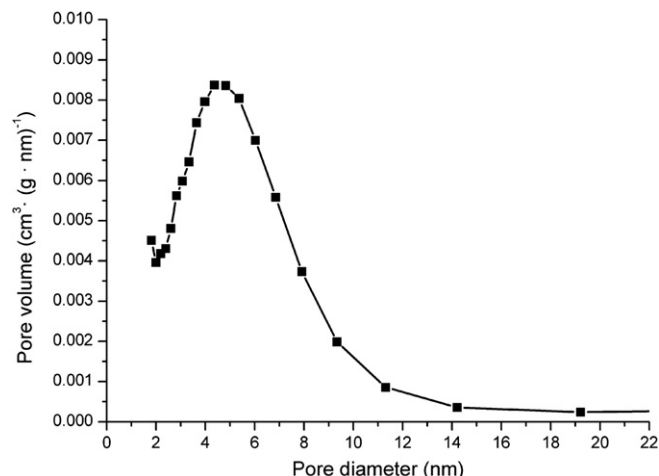


Fig. 2. Pore size distribution of the synthesized material measured from the nitrogen adsorption isotherm.

The cubic structure deduced from the electron diffraction correlates with Powder Diffraction Files #75-1002 ( $\text{W}_3\text{N}_4$  phase) and #25-1255 ( $\text{W}_{0.75}(\text{N},\text{O})$  phase). The crystal structure of the oxynitride  $\text{W}_{0.75}(\text{N},\text{O})$  is equivalent to that of  $\text{W}_3\text{N}_4$  but the elemental composition is different, with some nitrogen atoms in the crystal substituted by oxygen atoms in the oxynitride. A typical EELS spectrum collected from the sample (Fig. 4e) indicates the presence of the W, N and O elements. The distribution of these elements was analyzed by comparing bright-field TEM images with the corresponding EFTEM elemental maps of W, N and O (Fig. 4f). The elemental maps correlate well and, according to our results, W, N and O elements are all distributed throughout the sample. The distribution of O and N elements is inhomogeneous and the O/N atomic ratio varies between  $0.3$  and  $1$ . On the basis of the XRD and TEM data, the dominant phase in the synthesized material is tungsten oxynitride  $\text{W}_{0.75}(\text{N},\text{O})$ .

Electrochemical measurements, cyclic voltammetry and galvanostatic charge–discharge, demonstrate that tungsten oxynitride has capacitive properties in a range of aqueous electrolytes. Fig. 5 shows the CV curves of our material recorded at various scan rates in  $1$  M  $\text{H}_2\text{SO}_4$ . The graphs show a nearly ideal capacitive

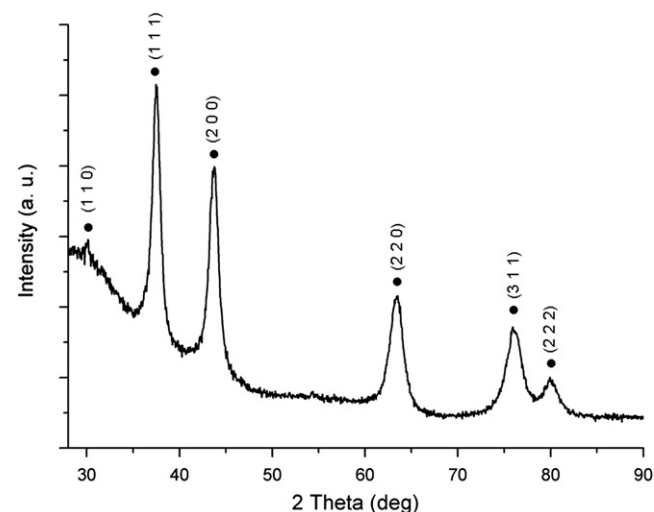


Fig. 3. XRD pattern of the synthesized powder. The symbol “●” denotes characteristic peaks of tungsten oxynitride.

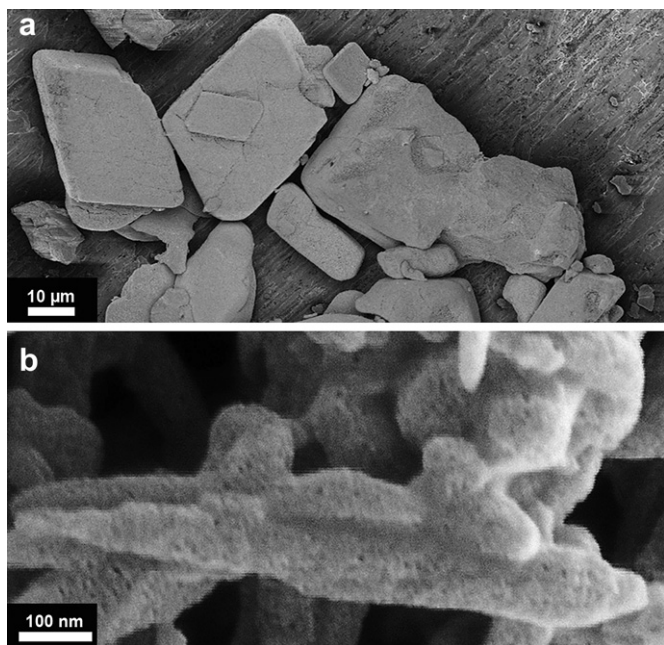
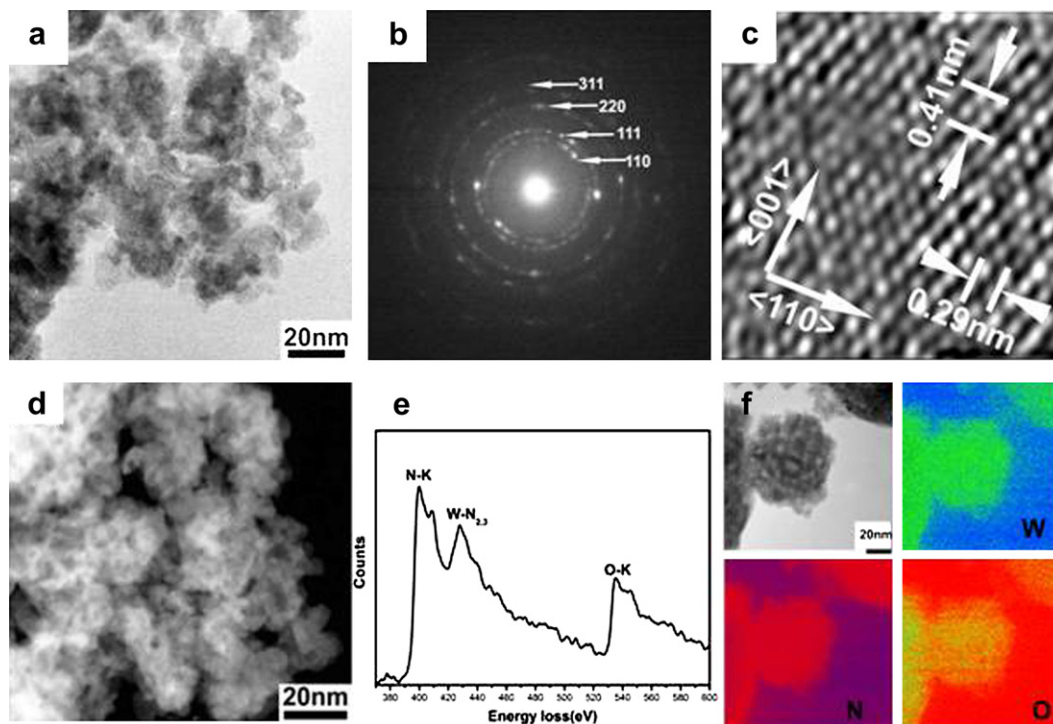


Fig. 1. Morphology of the synthesized powder: (a) a low magnification SEM image; (b) a high magnification SEM image highlighting the mesoporous structure of the particles.





**Fig. 4.** TEM characterization of the synthesized powder: (a) a bright-field image, (b,c) the corresponding electron diffraction pattern and high resolution image; (d) a high angle annular dark-field (HAADF) image highlighting the porous structure; (e) an EELS spectrum showing N, W and O edges; (f) a bright-field image and EFTEM maps of W, N and O elements.

behavior, with the shape of the CV curves being close to rectangular. The charge and discharge processes are, therefore, highly reversible in the acidic electrolyte. The capacitance value of  $85 \text{ F g}^{-1}$ , the highest among all electrolytes tested, was measured at a current load of  $0.05 \text{ A g}^{-1}$  using the galvanostatic charge–discharge method. The retention of capacitance at higher current rates (rate capability) is depicted in Fig. 6a. It follows from the graph that a tungsten oxynitride electrode is capable of preserving about 40% of the initial capacitance even after a 200-fold increase in the current density. A capacitance of  $33 \text{ F g}^{-1}$  is still retained when the applied current load is set to  $10 \text{ A g}^{-1}$ . The

charge–discharge profiles at current rates of  $0.5$  and  $5 \text{ A g}^{-1}$  are shown in Fig. 6b and c, respectively. Their shape is close to the ideal capacitive triangular shape, and the Coulombic efficiency of charge–discharge is, notably, close to 100%. The triangular shape of the charge–discharge profile is reasonably preserved at  $5 \text{ A g}^{-1}$ , although some IR drop (a quick shift in the measured potential upon switching the current to the opposite value) is evident. This may appear as a consequence of limitations of conductivity in the electrode, given that the electrode was assembled via the conventional procedure of mixing the active material with a conductive carbon component and an insulating binder.

Similar ideal shapes of CV curves were recorded for tungsten oxynitride in  $1 \text{ M KOH}$  electrolyte in the potential window of  $-1.1 \text{ V}$  to  $-0.3 \text{ V}$  vs  $\text{Hg/HgO}$  reference electrode. The specific capacitance value of  $57 \text{ F g}^{-1}$  was measured by galvanostatic charge–discharge at a current load of  $0.5 \text{ A g}^{-1}$ . The ideal electrochemical capacitive behavior in the same potential window has been reported previously for tungsten nitride phases [36,37]. Capacitances of 30 and  $100 \text{ F g}^{-1}$  have been measured, and the phases of the tungsten nitrides were assigned to tungsten mononitride  $\text{WN}$  [36] and tungsten nitride  $\text{W}_2\text{N}$  [37], respectively. Since the surface areas of our tungsten oxynitride and the materials described in the papers [36,37] are similar, the difference in capacitance values may arise from the stoichiometry and the exact nature of the crystalline phase.

Discussing the nature of the charge storage mechanism of  $\text{WN}$  and  $\text{W}_2\text{N}$  materials in  $1 \text{ M KOH}$ , Choi and Kumta [36] and Ko et al. [37] suggested that EDLC was the main charge storage mechanism. However, capacitance values of  $\sim 200 \mu\text{F cm}^{-2}$  and  $\sim 136 \mu\text{F cm}^{-2}$  are estimated in  $1 \text{ M H}_2\text{SO}_4$  and  $1 \text{ M KOH}$  electrolytes for mesoporous tungsten oxynitride with the specific surface area of  $42 \text{ m}^2 \text{ g}^{-1}$ . These values are significantly higher than  $20\text{--}50 \mu\text{F cm}^{-2}$  expected for the EDLC mechanism [5,6]. Recently, similar observations have been made for  $\beta\text{-W}_2\text{N}$  by Pande et al. [38]

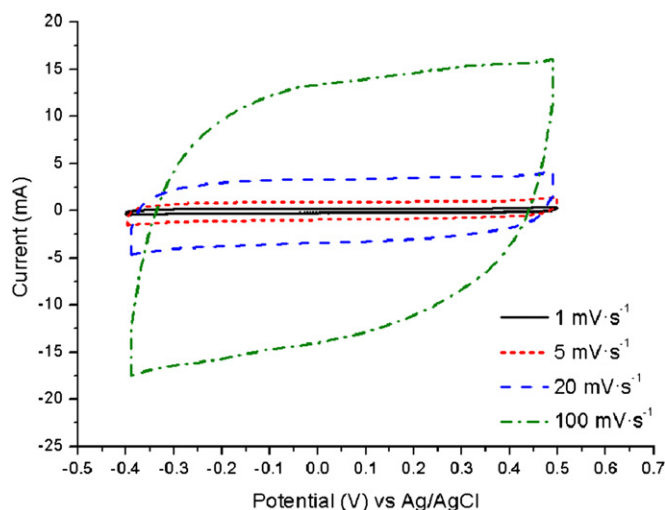


**Fig. 5.** Cyclic voltammogram (CV) curves of tungsten oxynitride in  $1 \text{ M H}_2\text{SO}_4$  aqueous electrolyte at different scan rates.

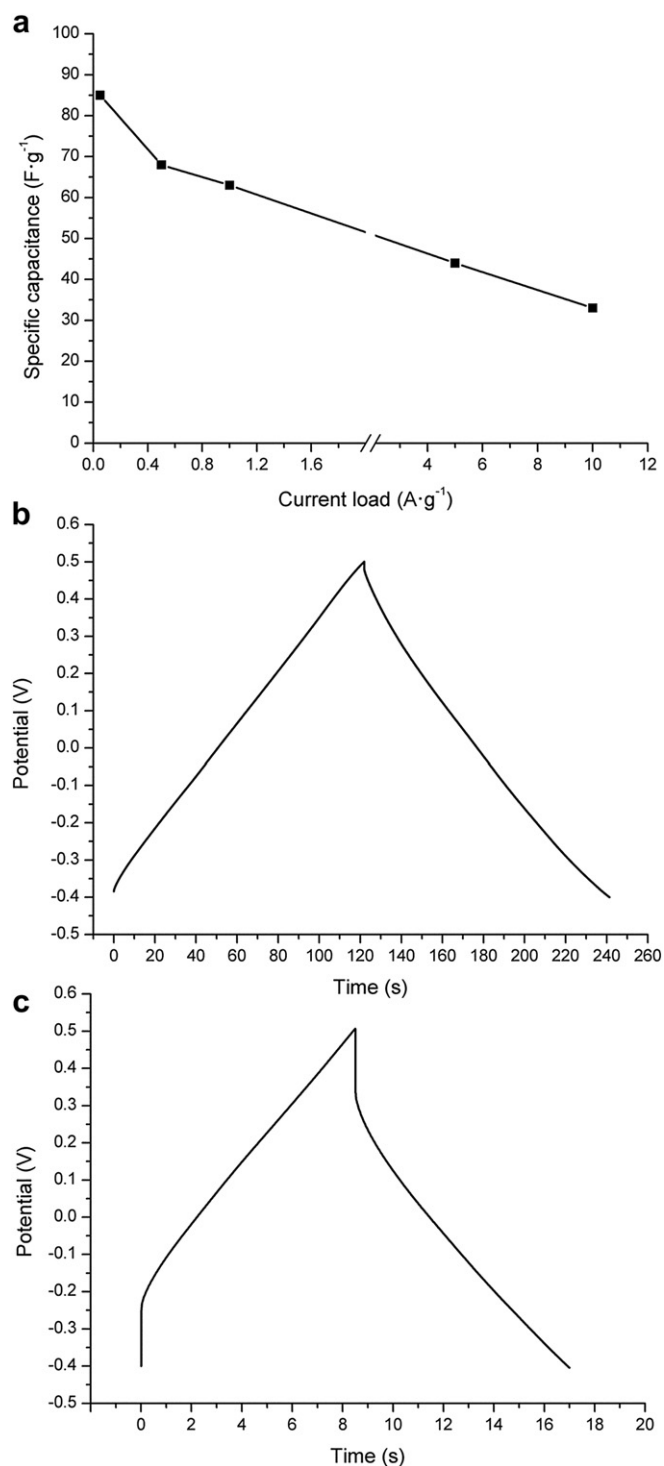


**Fig. 6.** Rate capability of tungsten oxynitride in 1 M  $\text{H}_2\text{SO}_4$  aqueous electrolyte (a) and galvanostatic charge and discharge curves at current rates of  $0.5 \text{ A g}^{-1}$  (b) and  $5 \text{ A g}^{-1}$  (c).

and the contribution of a pseudocapacitive charge storage mechanism has been proposed. We therefore conclude that the charge storage mechanism of tungsten oxynitride does not only result from the formation of the electric double-layer, but additionally involves pseudocapacitive processes.

The capacitive behavior is also observed in neutral aqueous solutions with different alkaline and alkaline-earth metal cations: 3 M KCl, 3 M NaCl, 1 M LiCl and 1 M  $\text{CaCl}_2$ . The corresponding CV

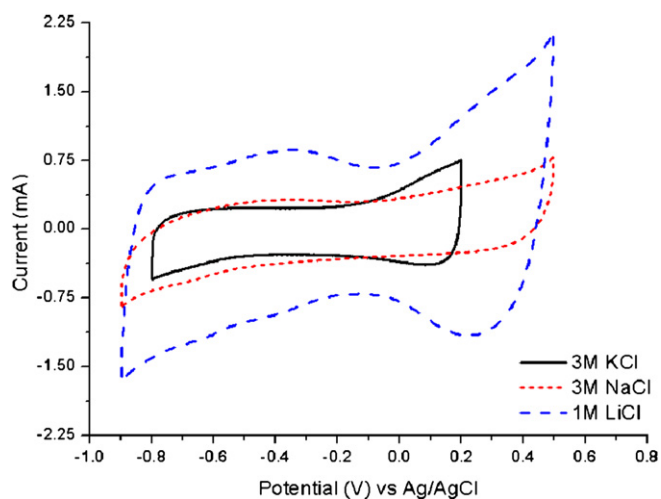


**Fig. 7.** CV curves of tungsten oxynitride in 3 M KCl, 3 M NaCl and 1 M LiCl aqueous electrolytes at a scan rate of  $5 \text{ mV s}^{-1}$ .

curves are shown in Figs. 7 and 8. This result indicates that tungsten oxynitride is not only working in the strong acid or alkaline media, but also in a range of non-corrosive electrolyte solutions. The CV shapes observed in neutral electrolytes are less rectangular than in 1 M  $\text{H}_2\text{SO}_4$  or 1 M KOH. The capacitance values measured by the galvanostatic charge–discharge method in the neutral electrolytes at the current load of  $0.5 \text{ A g}^{-1}$  are  $16 \text{ F g}^{-1}$  in 3 M NaCl,  $18 \text{ F g}^{-1}$  in 3 M KCl,  $28 \text{ F g}^{-1}$  in 1 M LiCl and  $39 \text{ F g}^{-1}$  in 1 M  $\text{CaCl}_2$ .

In order to evaluate the cyclic stability of the tungsten oxynitride electrodes, galvanostatic charge and discharge experiments were performed for multiple cycles in 1 M  $\text{H}_2\text{SO}_4$ , 3 M NaCl and 1 M KOH electrolytes at the current load of  $0.5 \text{ A g}^{-1}$ . The results are presented in Fig. 9. Furthermore, CV curves at the scan rate of  $5 \text{ mV s}^{-1}$  were measured after every 100 galvanostatic charge and discharge cycles (inserts in Fig. 9a–c). The performance of the tungsten oxynitride electrode is reasonably stable for the first 200 cycles and starts to degrade afterward in 1 M  $\text{H}_2\text{SO}_4$  electrolyte (Fig. 9a), while there is a faster loss of electrochemical reversibility in the neutral electrolyte (Fig. 9b). Due to the distortion of the discharge curves in 1 M  $\text{H}_2\text{SO}_4$  and 3 M NaCl electrolytes, experiments were discontinued after 300 and 400 galvanostatic charge

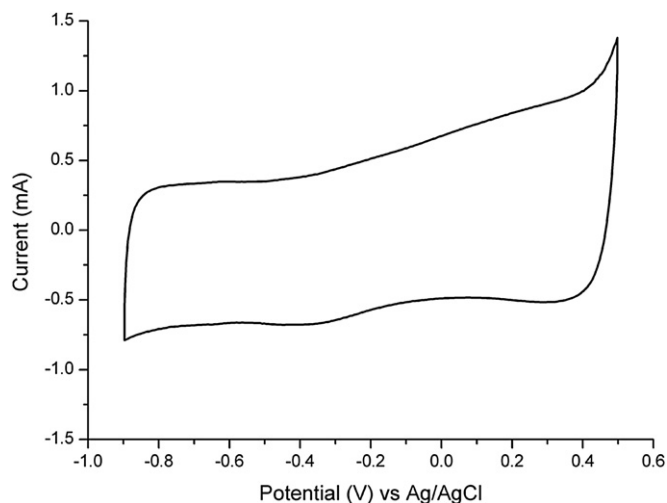


**Fig. 8.** CV curve of tungsten oxynitride in 1 M  $\text{CaCl}_2$  aqueous electrolyte at a scan rate of  $5 \text{ mV s}^{-1}$ .

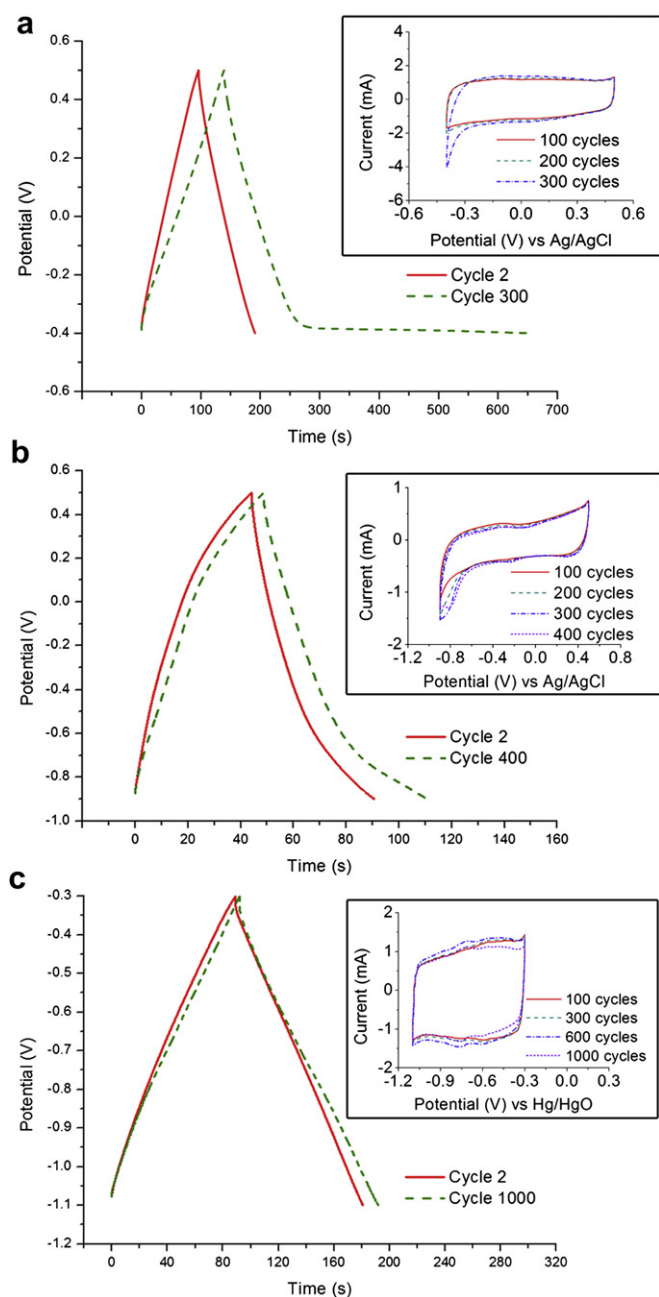


**Fig. 9.** Cyclic stability of tungsten oxynitride samples. Galvanostatic charge and discharge curves measured for the 2nd and 300th cycles in 1 M H<sub>2</sub>SO<sub>4</sub> electrolyte (a), for the 2nd and 400th cycles in 3 M NaCl electrolyte (b) and for the 2nd and the 1000th cycles in 1 M KOH electrolyte (c). Cyclic voltammetry curves measured after selected galvanostatic charge and discharge cycles are shown in inserts.

and discharge cycles, respectively. In 1 M KOH electrolyte, tungsten oxynitride electrode is reasonably stable for 1000 cycles (Fig. 9c). Minor increases in capacitance values (1 and 9%, respectively) between the first and the 1000th cycle were measured from the galvanostatic charge and discharge curves.

In order to investigate the influence of the electrolytes on the cyclic stability, the surface of the electrodes was characterized by XPS measurements after cycling in 1 M H<sub>2</sub>SO<sub>4</sub> and 1 M KOH electrolytes. Multiple galvanostatic charge and discharge cycles (>160 cycles) were performed in 1 M H<sub>2</sub>SO<sub>4</sub> and 1 M KOH solutions. The cycling was stopped when the discharge curve in 1 M H<sub>2</sub>SO<sub>4</sub> electrolyte became asymmetric. The W 4f spectra of the initial electrode

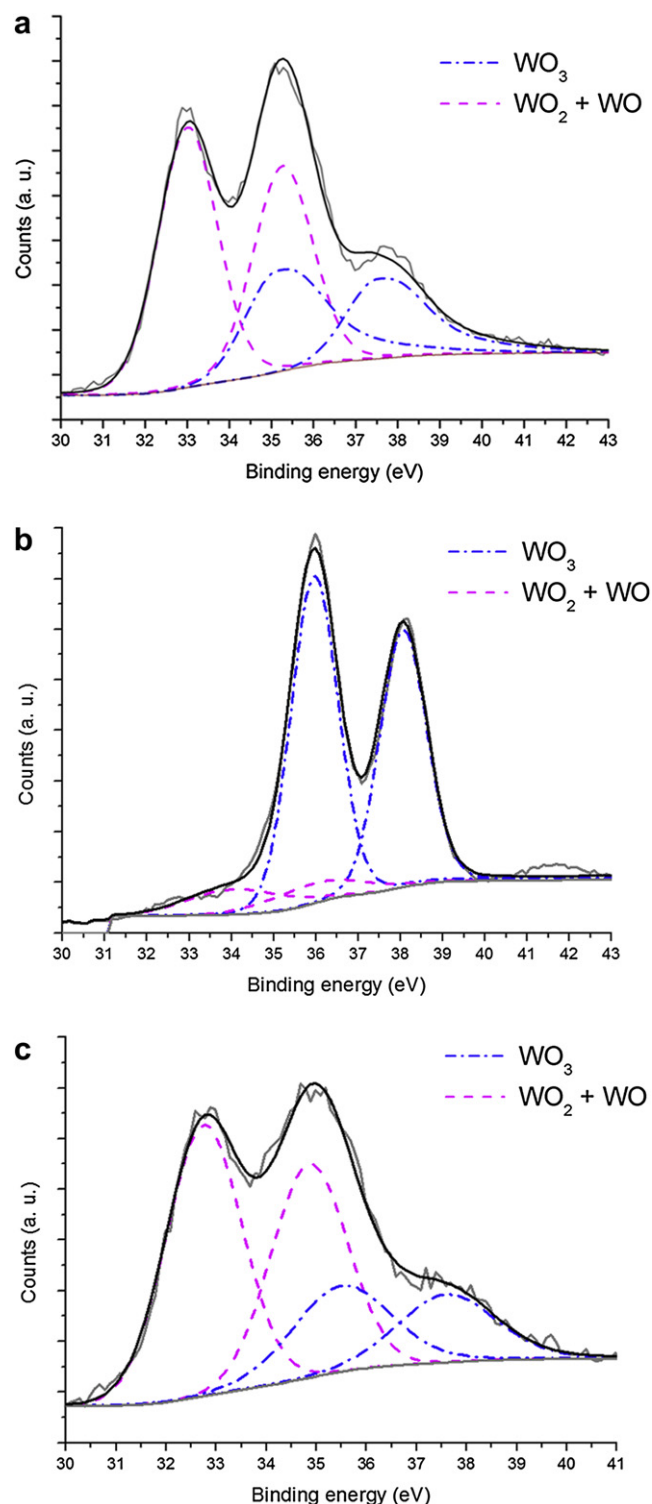


**Fig. 10.** Comparison of cyclic stability of tungsten oxynitride electrodes in 1 M H<sub>2</sub>SO<sub>4</sub> and 1 M KOH electrolytes: XPS spectra and deconvolution peaks of W 4f core levels. (a) Initial electrode; (b) electrode after cycling in 1 M H<sub>2</sub>SO<sub>4</sub> electrolyte and (c) after cycling in 1 M KOH electrolyte.

(Fig. 10a) were deconvoluted into four components on the basis of previously established binding energies in the XPS spectrum of tungsten oxynitride [39].

Two sets of W core levels are present. One consists of a doublet at 36.98 and 35.08 eV and corresponds to WO<sub>3</sub> species, while the

other is the doublet at 35.04 and 32.96 eV and relates to mixed  $\text{WO}_2$  and  $\text{WO}$  phases [39–41]. The  $\text{WO}_3$  and  $\text{WO}_2/\text{WO}$  doublets are shifted toward lower binding energies by about 1 eV and 0.5 eV, respectively, in comparison with the reference values, which might be caused by the high carbon content on the sample surface. It can be concluded that the surface of tungsten oxynitride is covered with a very thin passivating layer of oxides that cannot be identified by TEM measurements. This is in agreement with literature findings.  $\text{Ar}^+$  sputtering in the course of XPS measurement was needed to remove the upper layer of the surface of materials and reveal binding energies of 34.2 and 32.0 eV corresponding to mixed  $\text{W}_2\text{N}$  and  $\text{WN}$  phases [39,40]. When compared to the initial electrode (Fig. 10a), XPS spectra of the electrode cycled in 1 M  $\text{H}_2\text{SO}_4$  solution show an increased intensity of the peaks corresponding to the  $\text{WO}_3$  species (Fig. 10b), while in KOH, the XPS spectra remain nearly unchanged (Fig. 10c). The results demonstrate that the surface of the electrodes becomes progressively oxidized in 1 M  $\text{H}_2\text{SO}_4$  solution, while it remains similar to the surface of the initial electrode in 1 M KOH. These data are in agreement with observations by Pande et al. [38], who reported good stability of VN and  $\beta\text{-W}_2\text{N}$  in the KOH electrolyte.

Two typical charge storage mechanisms have been proposed for materials possessing the pseudocapacitive behavior, such as  $\text{MnO}_2$ , in aqueous electrolytes: pseudocapacitive ion/proton adsorption on the surface [18,26] and ion/proton intercalation into the crystal lattice [22–24] of the active material. As a part of the preliminary assessment of the possible pseudocapacitive mechanism in tungsten oxynitride, we assume that one of these two mechanisms may be applicable to this material. Accordingly, additional XRD measurements were performed to investigate bulk and surface changes in the electrodes in 1 M  $\text{H}_2\text{SO}_4$  and 3 M KCl electrolytes.

Figs. 11 and 12 show the XRD patterns of the initial tungsten oxynitride electrode and the electrodes stopped in the discharged and charged states in the 10th cycle in 1 M  $\text{H}_2\text{SO}_4$  and 3 M KCl electrolytes. It is obvious from the data that no changes in the characteristic peak positions or full widths at half maximum (FWHM) are visible (Figs. 11b and 12b) when patterns of the initial material and those of materials after cycling are compared. No changes in the bulk crystalline structure or no loss of crystallinity can be detected. If the mechanism of intercalation is involved in charge storage, it is normally accompanied by expansion and shrinkage of the lattice and, consequently, by changes in the XRD

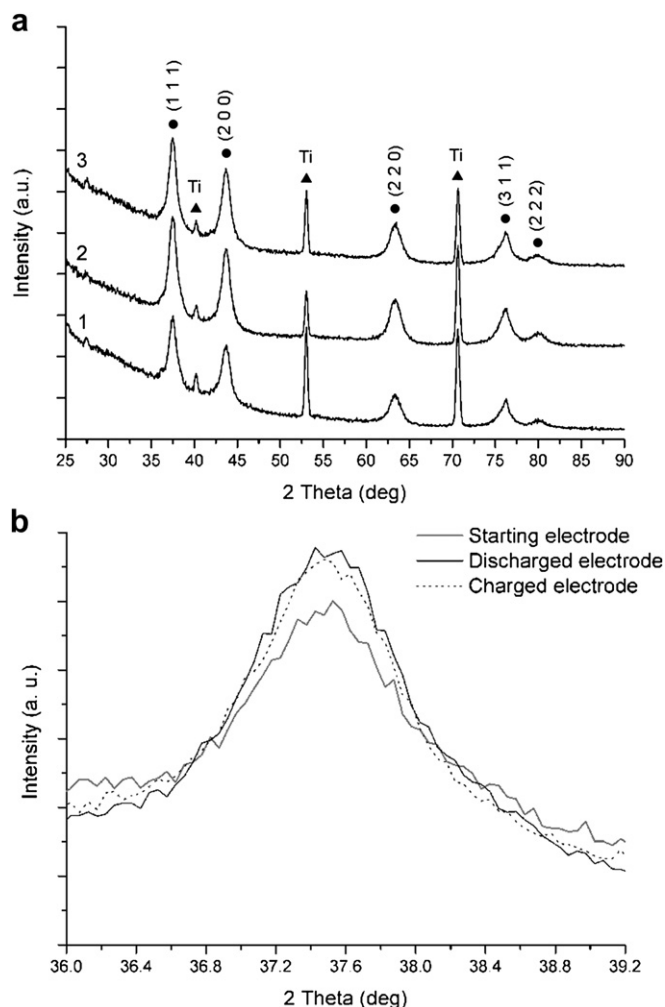


**Fig. 11.** (a) XRD patterns of the initial tungsten oxynitride electrode (pattern 1), electrode discharged to -0.4 V vs Ag/AgCl reference electrode in the 10th cycle (pattern 2) and electrode charged to 0.5 V vs Ag/AgCl reference electrode in the 10th cycle (pattern 3) in 1 M  $\text{H}_2\text{SO}_4$  electrolyte. ● – characteristic peaks of tungsten oxynitride; ▲ – the peaks corresponding to the Ti current collector. (b) The magnified (111) diffraction peaks.

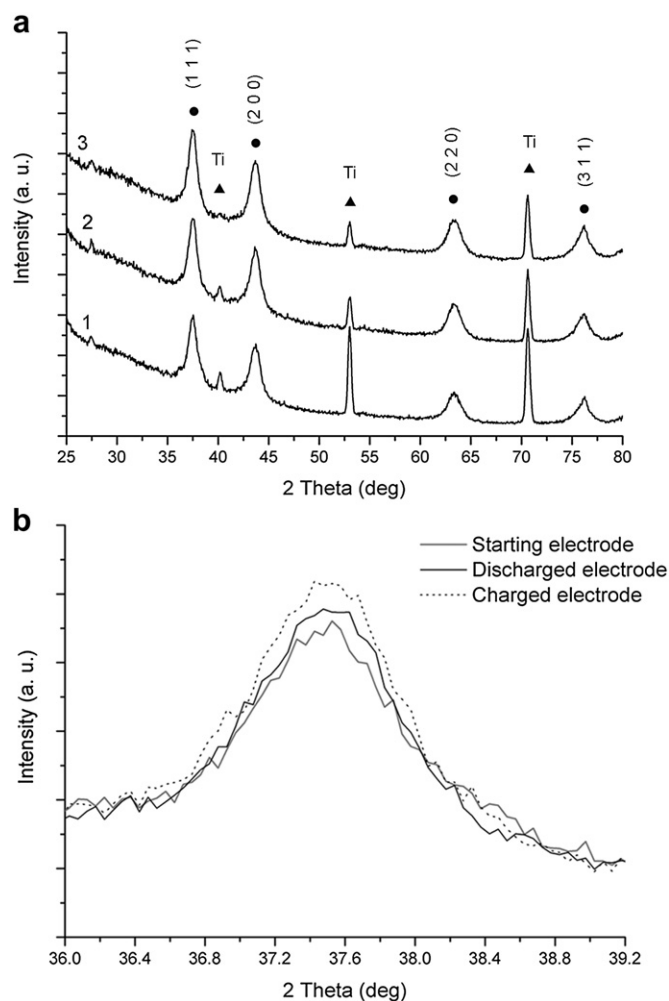


**Fig. 12.** (a) XRD patterns of the initial tungsten oxynitride electrode (pattern 1), electrode discharged to -0.8 V vs Ag/AgCl reference electrode in the 10th cycle (pattern 2) and electrode charged to 0.2 V vs Ag/AgCl reference electrode in the 10th cycle (pattern 3) in 3 M KCl electrolyte. ● – characteristic peaks of tungsten oxynitride; ▲ – the peaks corresponding to the Ti current collector. (b) The magnified (111) diffraction peaks.



patterns of the active material in the charged and discharged states. For example, intercalation of cations into crystalline  $\text{MnO}_2$  is accompanied by a reversible shift of its XRD peaks [21,22]. The lack of changes in the XRD patterns of the electrodes is evidence that no bulk intercalation takes place. The pseudocapacitive adsorption of protons or cations is, however, a possible mechanism and agrees with the absence of any bulk transformations in tungsten oxynitride.

#### 4. Conclusions

Mesoporous tungsten oxynitride has been synthesized by temperature-programmed reduction of tungsten oxide powder. The phase composition has been analyzed by XRD, TEM and EELS. The  $\text{W}_{0.75}(\text{N},\text{O})$  phase of tungsten oxynitride is assigned as the phase with the best match of the elemental composition and crystallographic parameters of the material. The tungsten oxynitride consists of mesoporous macroscopic particles possessing a pore size distribution with a maximum at around 6 nm.

The electrochemical capacitance of tungsten oxynitride is observed in a range of aqueous electrolytes – 1 M  $\text{H}_2\text{SO}_4$ , 1 M KOH, 3 M KCl, 3 M NaCl, 1 M LiCl and 1 M  $\text{CaCl}_2$ . Notably, the charge–discharge and cyclic voltammetry curves with ideal shapes (close to triangular and square, respectively) are recorded in the aqueous 1 M  $\text{H}_2\text{SO}_4$  and 1 M KOH electrolytes, and capacitance values of 85 and 57  $\text{F g}^{-1}$  are measured in these electrolytes. The capacitance values vary in different electrolytes and are dependent on the presence of particular cations. Cyclic stability studies have been performed in a range of electrolytes and the highest stability is observed in 1 M KOH electrolyte. Ion adsorption and ion intercalation were considered as two possible key mechanisms of pseudocapacitive contribution. We conclude that the bulk intercalation of protons or cations into tungsten oxynitride does not occur while pseudocapacitive ion adsorption is a possible mechanism. XPS measurements show that the surface of tungsten oxynitride is covered with a thin layer composed of  $\text{WO}_3$  and  $\text{WO}_2/\text{WO}$  species, and the ratio of these species varies upon electrochemical testing in different electrolytes.

#### Acknowledgments

This research project is supported by the ARC Centre of Excellence for Functional Nanomaterials and a grant from Deakin University (Central Research Grant Scheme). The authors thank Mr. Robert Lovett and Dr. Andrew Sullivan for their help. The authors also acknowledge valuable discussions with Prof. Johan du Plessis and access to the XPS facility at RMIT University. The work at the School of Physics and the Center for Research on Adaptive Nanostructures and Nanodevices at Trinity College Dublin is supported by Science Foundation Ireland under Grant 07/SK/I1220a. Dr. Yanhui Chen appreciates support from IRCSET and Solarprint Ireland (C1917). The TEM work was conducted under the framework of the

INSPIRE programme, funded by the Irish Government's Programme for Research in Third Level Institutions, Cycle 4, National Development Plan 2007–2013.

#### References

- [1] M. Conte, Fuel Cells 10 (2010) 806–818.
- [2] A. Burke, J. Power Sources 91 (2000) 37–50.
- [3] A.I. Belyakov, D.A. Sojref, International Conference on Power Engineering, Energy and Electrical Drives, IEEE, New York, 2009, pp. 337–341.
- [4] R. Kötz, M. Carlen, Electrochim. Acta 45 (2000) 2483–2498.
- [5] B.E. Conway, V. Birss, J. Wojtowicz, J. Power Sources 66 (1997) 1–14.
- [6] A.G. Pandolfo, A.F. Hollenkamp, J. Power Sources 157 (2006) 11–27.
- [7] B.E. Conway, J. Electrochem. Soc. 138 (1991) 1539–1548.
- [8] J.P. Zheng, P.J. Cygan, T.R. Jow, J. Electrochem. Soc. 142 (1995) 2699–2703.
- [9] P. Simon, Y. Gogotsi, Nat. Mater. 7 (2008) 845–854.
- [10] X. Zhao, B.M. Sánchez, P.J. Dobson, P.S. Grant, Nanoscale 3 (2011) 839–855.
- [11] A. Rudge, J. Davey, I. Raistrick, S. Gottesfeld, J.P. Ferraris, J. Power Sources 47 (1994) 89–107.
- [12] M. Wixom, L. Owens, J. Parker, J. Lee, I. Song, L. Thompson, in: Proceedings of the Symposium on Electrochemical Capacitors II, vol. 96, 1997, pp. 63–74.
- [13] D. Choi, P.N. Kumta, J. Am. Ceram. Soc. 94 (2011) 2371–2378.
- [14] D. Choi, G.E. Blomgren, P.N. Kumta, Adv. Mater. 18 (2006) 1178–1182.
- [15] X.L. Li, Y. Xing, H. Wang, H.L. Wang, W.D. Wang, X.Y. Chen, Trans. Nonferrous Met. Soc. China 19 (2009) 620–625.
- [16] D. Choi, P.N. Kumta, J. Electrochem. Soc. 153 (2006) A2298–A2303.
- [17] C. Xu, F.Y. Kang, B.H. Li, H.D. Du, J. Mater. Res. 25 (2010) 1421–1432.
- [18] H.Y. Lee, V. Manivannan, J.B. Goodenough, C. R. Acad. Sci. Ser. IIC: Chim. 2 (1999) 565–577.
- [19] R.N. Reddy, R.G. Reddy, J. Power Sources 124 (2003) 330–337.
- [20] Y.U. Jeong, A. Manthiram, J. Electrochem. Soc. 149 (2002) A1419–A1422.
- [21] S.L. Kuo, N.L. Wu, J. Electrochem. Soc. 153 (2006) A1317–A1324.
- [22] L. Athouël, F. Moser, R. Dugas, O. Crosnier, D. Bélanger, T. Brousse, J. Phys. Chem. C 112 (2008) 7270–7277.
- [23] H. Kanoh, W.P. Tang, Y. Makita, K. Ooi, Langmuir 13 (1997) 6845–6849.
- [24] O. Ghodbane, J.L. Pascal, F. Favier, ACS Appl. Mater. Interf. 1 (2009) 1130–1139.
- [25] C.J. Xu, C.G. Wei, B.H. Li, F.Y. Kang, Z.C. Guan, J. Power Sources 196 (2011) 7854–7859.
- [26] D. Bélanger, M. Toupin, T. Brousse, Chem. Mater. 14 (2002) 3946–3952.
- [27] P. Ragupathy, H.N. Vasan, N. Munichandraiah, J. Electrochem. Soc. 155 (2008) A34–A40.
- [28] S. Devaraj, N. Munichandraiah, J. Phys. Chem. C 112 (2008) 4406–4417.
- [29] T. Brousse, M. Toupin, R. Dugas, L. Athouël, O. Crosnier, D. Bélanger, J. Electrochem. Soc. 153 (2006) A2171–A2180.
- [30] M. Toupin, T. Brousse, D. Bélanger, Chem. Mater. 16 (2004) 3184–3190.
- [31] S.C. Pang, M.A. Anderson, T.W. Chapman, J. Electrochem. Soc. 127 (2000) 444–450.
- [32] J. Yan, Z.J. Fan, T. Wei, J. Cheng, B. Shao, K. Wang, L.P. Song, M.L. Zhang, J. Power Sources 194 (2009) 1202–1207.
- [33] Y. Lei, C. Fournier, J.L. Pascal, F. Favier, Microporous Mesoporous Mater. 110 (2008) 167–176.
- [34] L.E. Toth, Transition Metal Carbides and Nitrides, Academic Press, New York, 1971.
- [35] T.E. Lucy, T.P. St. Clair, S.T. Oyama, J. Mater. Res. 13 (1998) 2321–2337.
- [36] D. Choi, P.N. Kumta, J. Am. Ceram. Soc. 90 (2007) 3113–3120.
- [37] A.R. Ko, S.B. Han, Y.W. Lee, K.W. Park, Phys. Chem. Chem. Phys. 13 (2011) 12705–12707.
- [38] P. Pande, P.G. Rasmussen, L.T. Thompson, J. Power Sources 207 (2012) 212–215.
- [39] D.H. Cho, T.S. Chang, C.H. Shin, Catal. Lett. 67 (2000) 163–169.
- [40] Y.M. Zhao, W.B. Hu, Y.D. Xia, E.F. Smith, Y.Q. Zhu, C.W. Dunnill, D.H. Gregory, J. Mater. Chem. 17 (2007) 4436–4440.
- [41] T. Nakajima, K. Watanabe, N. Watanabe, J. Electrochem. Soc. 134 (1987) 3175–3178.